Deep-Level Defects in CdZnTe and CdMnTe Detectors Identified by Photo-Induced Current Transient Spectroscopy (PICTS) and Thermally Simulated Current (TSC) Techniques

P. Vigneshwara Raja

Deep-Level Defects in $Cd_{1-x}Zn_xTe$ and $Cd_{1-x}Mn_xTe$ Detectors Identified by Photo-Induced Current Transient Spectroscopy (PICTS) and Thermally Simulated Current (TSC) Techniques

Postdoc Report Submitted by

P. Vigneshwara Raja

Under the supervision of

Prof. Arie Ruzin

Team Members

Artem Brovko and Anastasiia Adelberg

Department of Physical Electronics
School of Electrical Engineering
Faculty of Engineering
Tel Aviv University
69978 Tel Aviv
Israel

Abstract:

The deep-level defects in the $Cd_{1-x}Zn_xTe$ (CZT) and $Cd_{1-x}Mn_xTe$ (CMT) detectors are characterized by photo-induced current transient spectroscopy (PICTS), thermoelectric emission spectroscopy (TEES) and thermally stimulated current (TSC) measurements. Two different types of CZT crystals are considered for trap characterization; the first type is grown by using vertical Bridgman (VB) method and treated with oxygen plasma for surface passivation, whereas the second type is grown by the VB arrangement with accelerated crucible rotation technique (ACRT). The CMT samples used in defect characterization studies are grown by the VB method. The deep-level donor responsible for the electrical compensation in the CZT and CMT bulk is identified from the steady-state thermal generation current characteristics. From the PICTS and TEES results, the trap signatures in the various CZT and CMT detectors are analyzed and compared in terms of their energy level, capture cross-section, and carrier detrapping time of the defects. Furthermore, DC photoconductivity measurements are conducted to assess the carrier mobility-lifetime ($\mu\tau$) product in the CZT and CMT crystals. The midgap states at 0.81-0.85 eV are found in all the CZT and CMT crystals and these deep-level traps should play a significant role in carrier compensation along with the deep-level donors (E_{DD} = 0.78-0.84 eV). To the best of our knowledge, three new traps at E_V + 0.22 eV, E_C - 0.68 eV and E_C - 0.7 eV are identified in the CMT crystals for the first time in the literature. The reported deep-level defects are intended to provide excellent feedback to the CZT and CMT bulk growth community for the radiation detector technology developments.

Keywords: CdZnTe, CdMnTe, deep-level defects, PICTS, TEES, TSC.

1. Introduction

Cadmium zinc telluride ($Cd_{1-x}Zn_xTe$ or CZT) detectors have been utilized for room temperature X- and γ-ray imaging applications due to its superior physical properties such as high-Z atomic number (high absorption efficiency), wide bandgap, and reasonable electron mobility-lifetime ($\mu\tau$) products [1-3]. However, CZT crystals have some limitations such as low Zn solubility and low $\mu\tau$ product for holes [4,5]. Cadmium manganese telluride ($Cd_{1-x}Mn_xTe$ or CMT) is another promising material suitable for room temperature radiation detectors [6-9]. In fact, CMT has several advantages over its competitor CZT [6-9]: First, the bandgap of MnTe (~3.2 eV) is much higher than ZnTe (~2.2 eV), so lower Mn concentration is required to attain the desired bandgap (compared to Zn content in CZT) and broader bandgap tunability (1.7-2.2 eV). Second benefit, almost homogenous distribution of Mn in the ingot is anticipated due to the near-unity segregation coefficient of Mn in CdTe, where the Zn segregation coefficient in CdTe is ~1.35. The vertical Bridgman (VB) is one of the commonly used bulk growth techniques to produce single crystalline CZT and CMT [1,3,9-11]. The high resistivity ($\rho > 10^9$ Ω cm) CZT and CMT substrates are obtained through the compensation of native acceptors (Cd vacancies) by the introduction of deep-level donor dopants [1-3,6,11]. The main challenge in developing CZT and

CMT radiation detectors lies in growing single crystals which are free from defects viz. Te inclusions, precipitates, dislocations, twins, and sub-grain boundaries [8-13]. The crystal defects and impurities introduce electrically active defects inside the bandgap and hinder the charge transport properties of the detector via trapping phenomena [1-3,8,13]. Hence, identification of deep-level defects in the CZT and CMT crystals is an important step in improving the detector energy resolution and charge collection efficiency. Therefore, the current work is targeted to identify the traps in the CZT and CMT detectors.

The as-grown CZT crystals are treated with oxygen plasma in order to reduce the detector leakage current; this process is known as surface passivation using oxygen plasma [14-16]. The presence of Te flux inclusions in the CZT detectors introduces significant charge trapping and distort the internal electric field lines (polarization), thereby degrading the detector performance [17-19]. Mccoy *et al.* [18-19] mitigated the flux inclusion formation in the CZT ingot by the application of accelerated crucible rotation technique (ACRT) to melt mixing in the VB configuration (i.e. VB-ACRT). Taking these points into account, the above two types of CZT crystals are used in this work. The defects in the VB-grown CZT crystals (oxygen plasma treated) are characterized along with the CZT samples grown by the VB-ACRT system. From the results, various defects present in these two different types of CZT are analyzed. In comparison with the CZT [20-56], the trap levels present in the CMT crystals are not well reported in the literature [57-67]. Kim *et al.* [63] investigated the defects in the detector-grade CZT and CMT crystals grown by the VB technique and found some of the similar trap activation energies at 10-12 meV, 0.35-0.37 eV, 0.71-0.78 eV, 1.06-1.09 eV in both the materials. Recently, Luan *et al.* [67] applied thermally stimulated current (TSC) and photoluminescence (PL) techniques to detect the deep-level defects in the vanadium (V) doped $Cd_{0.9}Mn_{0.1}Te$ single crystals grown by VB method. In the focus of providing further data to the CMT community, the deep-level traps in the VB grown CMT samples are identified in this work.

A powerful technique, namely photo-induced current transient spectroscopy (PICTS) [20-29, 68] is used to acquire the quantitative information about deep-level traps in the high resistivity CZT and CMT materials. To complement the PICTS results and to distinguish the electron and hole traps in the CZT and CMT samples, thermoelectric emission (or effect) spectroscopy (TEES) [30-33, 69-71] measurements are carried out. The thermally stimulated current (TSC) measurements are also conducted on the CZT and CMT samples. The deep-level donor (E_{DD}) responsible for the bulk compensation is identified from the steady-state thermal generation current measurements [36,37,45,46,50]. The carrier detrapping time of the defects is computed from the identified trap activation energy and capture cross-section [27-29]. Moreover, the carrier mobility-lifetime ($\mu\tau$) product in the CZT and CMT crystals is estimated by the direct current (DC) photoconductivity measurements [29,65,72-75] conducted using 650 nm laser light. The deep-level defects observed in the various CZT and CMT samples are intended to provide excellent feedback to the crystal growth engineers for further development in the CZT and CMT detector technologies.

2. Experiment

Two numbers (labeled as CZT-1 and CZT-2) of oxygen plasma treated VB-grown CZT crystals [76] were used for the initial trap characterization. To detect the deep-levels in the VB-ACRT grown CZT crystals [17-19], another two samples (CZT-W3 and CZT-W4) were used for this purpose. Three numbers of VB-grown CMT crystals (CMT-1, CMT-2 and CMT-3) [76] were also utilized in this work. Among these samples, the CMT-1 crystal was oxygen plasma treated, while the other CMT samples (CMT-2 and CMT-3) were found to be plasma-free.

2.1. CZT and CMT device fabrication

The content of zinc in all CZT samples was specified as ~ 5% atomic. The atomic content of Mn in CMT crystals was about 3.5 %.

The spatial dimensions of CZT-1, CZT-2 and CMT-1 were approximately 20 x 20 x 5 mm^3, while the other CMT samples (CMT-2 and CMT-3) had dimensions of 10 x 10 x 5 mm^3. The CZT-W3 and CZT-W4 samples were rather thinner with the dimensions of 10 x 10 x 2 mm^3.

All samples (both from CZT and CMT group) provided by GE passed a post-growing annealing step. The so-called "plasma-treated" samples CZT-1, CZT-2 and CMT-1 underwent an oxidation processing of the top surface in Diener Plasma system. Afterwards they remained untouched at room temperature conditions for approximately 30 months. The effect of "aging" and plasma deep penetration for the plasma-treated samples and its impact on the devices' properties is described in detail at [16]. The CMT-2 and CMT-3 samples underwent the plasma processing as well but were almost immediately taken into research process with the mechanical erase of the plasma affected surface layers. Thus, we consider them to be free of any plasma affection.

The surface processing for the samples CZT-1, CZT-2, CMT-1 and CMT-2 included a mechanical polishing with 1 μm alumina powder on a special tissue pad with a removing of about 40 μm layer from top and bottom surfaces. The CMT-3 crystal was polished in the same manner and was etched in 2% Bromine Methanol solution for 2 minutes right after the polishing step. The CZT-W3 and CZT-W4 samples were polished with 1 μm Al_2O_3 powder likewise the CZT-1 and CZT-2 samples.

The surface treatment was followed by the metallization step. In case of samples namely CZT-1, CZT-2, CMT-1, CMT-2, CMT-3, the indium 100 nm thick contacts were deposited via thermal vacuum evaporation method at 10^{-6} Torr on both top and bottom surfaces, resulting in M-S-M (metal-semiconductor-metal) structures. The contact patterning exhibits a fully covered bottom surface and a 5 x 5 mm^2 contact centralized on the top crystal surface.

In case of CZT-W3 and CZT-W4 samples, instead of indium contacts, the 100 nm thick gold contacts were deposited using vacuum thermal evaporation method. The contact design for top and

bottom surfaces was the similar: a square contact covering the whole surface except the 1 mm gap from the crystal edges. In order to conduct measurements, the studied samples were mounted on the ceramic holders with metallized area, enabling an electrical connection to the measuring setup.

2.2. PICTS characterization

The device under test (DUT) was placed on a sample holder in the liquid-nitrogen cooled LT4 Helitran® cryostat equipped with an optically transparent entrance window. Cernox® sensor was attached to the sample holder and its temperature was controlled and monitored by Lakeshore 325 temperature controller. The DUT was illuminated using red laser diode module with excitation wavelength of 650 nm and optical power of 100 mW. A constant bias voltage (V_B) of either -50 V or +50 V (polarity relative to top contact) was applied to induce electron or hole injection in the DUT during the PICTS measurements. It is expected that 650 nm (1.9 eV) wavelength light absorbs near the illumination surface of the CZT and CMT and generates electron-pairs there; according to the bias polarity, either electron or hole should drift towards the crystal volume until they get trapped or recombined [68]. The traps in the DUT were populated at each temperature by 1 ms long laser pulses. As soon as the laser source was turned off, free excess carriers (yet not trapped) exist in the bulk were quickly evacuated (possibly in several μs) due to the applied voltage, thereafter the de-trapped charge contribution dominates the current transients obtained for the time duration of 200 ms. The current transients were amplified with a sensitivity of 10^{-7} A/V using low noise Ithaco 1211 current preamplifier and the current compression control was adjusted to eliminate the DC current component in the transient. The amplifier output signals were transformed into equivalent digital signals using NI SCB-68 shielded I/O connector and were simultaneously recorded in the PC. The current transients were acquired in the temperature range of 80-400 K by varying the sample temperature. The lock-in method [77] was adopted for the transient analysis; here only a part of the transient was evaluated based on the rate window (e_m). In the selected fraction of the transient (T_C), the sum of last 40% portion (0.6 T_C to 1 T_C) of the transient signal was deducted from the sum of 0.1 T_C - 0.5 T_C of the transient, consequently the PICTS signal was attained for the particular rate window. In the same way, the PICTS spectra were acquired for six different rate windows such as 10 s^{-1}, 20 s^{-1}, 35 s^{-1}, 50 s^{-1}, 100 s^{-1}, and 200 s^{-1}, respectively.

2.3. TEES and TSC characterization

The main difference between thermoelectric emission spectroscopy (TEES) and the well-known thermally stimulated current (TSC) measurements is the driving force used for the movement of charge carriers during the thermal ramp-up [30,31,71]. In both experiments, the DUT was cooled down to a low temperature of ~80 K (T_0) without any bias voltage. Upon reaching T_0, the electrically active defects in the DUT were populated using 650 nm light illumination under the bias voltage for the time duration of 200 s. Two different bias voltages (V_B) of either -50 V or +50 V were employed in the laser pumping

step to obtain electron or hole population conditions in the DUT. Finally, the sample temperature was increased at the heating rate of 0.2 K/s and the thermal emission current was measured under dark conditions using Keithley 6517A Electrometer. No bias voltage was applied to the DUT throughout the TEES experiments (including warm-up). As the heater is mounted on the sample holder, the bottom electrode of the sample is at a higher temperature than the top contact during the thermal ramp-up, as a result the de-trapped electrons and holes force to move towards the colder electrode and the resultant electron and hole currents have opposite signs [30,31,71]. Therefore, the TEES technique can differentiate the electron and hole traps in the CZT and CMT samples. The TEES was used as the complementary to the PICTS for the purpose of trap identification. During the TSC thermal scan, the DUT was kept under a bias voltage (V_B = -10 V or +10 V), so the de-trapped electrons and holes drift towards the opposite electrodes due to the applied electric field and the resulting electron and hole currents have the same sign [31,78]. Hence, TSC spectroscopy cannot discriminate the electron and hole traps in the sample, however the TSC signal magnitude is stronger than the TEES.

The thermal generation of carriers via deep-level donors (responsible for electrical compensation in the CZT and CMT crystals) essentially governs the TSC spectrum acquired above room temperature [45,46]. To identify the deep-level donor (E_{DD}), the steady-state thermal generation current was measured under V_B = -10 V without laser excitation (no trap filling).

2.4. DC photoconductive measurement

The DC photoconductivity technique is relatively simple and well-established method used for decades to assess the $\mu\tau$ product in the CZT and CMT samples [29,65,72-75]. At room temperature, the photoconductivity measurement was conducted by using the 650 nm laser employed in the PICTS experiment. The top contact of the DUT was illuminated, and the resulting photocurrent was measured with the respect to the applied negative bias voltages (V_B = 0 V to -200 V). In this configuration, the electron current contribution may dominate the photocurrent responses. The effective value of the $\mu\tau$ product was estimated by fitting the photoconductivity current with the Hecht equation [29,65,72-75].

3. Results and Discussion

3.1. Traps in VB grown CZT crystals

Figure 1 shows the PICTS acquired at the rate window $e_m = 10\ s^{-1}$ for the VB grown oxygen-plasma treated CZT-1 sample under two bias conditions such as V_B = -50 V (preferential electron injection) and +50 V (preferential hole injection). There are seven distinct peaks seen in the PICTS of Fig. 1: A1, A2, A3, A4 at -50 V and A5, A6, A7 under +50 V. The peak maximum position is found to shift towards higher temperatures with the increasing rate window, i.e. PICTS follows the Arrhenius law. The peak maximum temperature (T_m) of the peaks is noted at different rate windows and are related with activation energy (E_T) and capture cross-section (σ) by the Arrhenius expression [68,79]:

$$\ln\left(\frac{T_m^2}{e_m}\right)=\frac{E_T}{kT_m}-\ln\left(\frac{\sigma N_C v_{th}}{gT_m^2}\right) \quad (1)$$

where N_C is the effective density of states for conduction band for electron trap, v_{th} is the carrier thermal velocity, and g is the degeneracy factor. Figure 2 depicts the Arrhenius plots of $ln(T_m^2/e_m)$ versus $1/kT_m$ for the peaks A1-A7 observed in the CZT-1. The activation energies and capture cross sections are calculated from the slope and intercept of the Arrhenius plots: A1 (0.12±0.01 eV, 3×10^{-17} cm^2), A2 (0.19±0.02 eV, 1×10^{-17} cm^2), A3 (0.64±0.04 eV, 3×10^{-14} cm^2), and A4 (0.85±0.03 eV, 5×10^{-13} cm^2) for -50 V; and A5 (0.24±0.02 eV, 7×10^{-16} cm^2), A6 (0.61±0.02 eV, 4×10^{-14} cm^2), and A7 (0.85±0.03 eV, 6×10^{-13} cm^2) for +50 V. Note that, the trap signatures for the peaks A4 and A7 are quite similar, so these peaks might be produced by the same defect. However, these peaks A4 and A7 are observed in both bias conditions, which reveal that the electron (V_B = -50V) and hole (V_B = +50V) injection into the bulk is always mixed (asymmetric carrier injection). In this case, it may not be possible to distinguish the electron and hole traps from the PICTS results even at two different bias configurations. Hence, the TEES results are used to identify the trap type in the CZT and CMT.

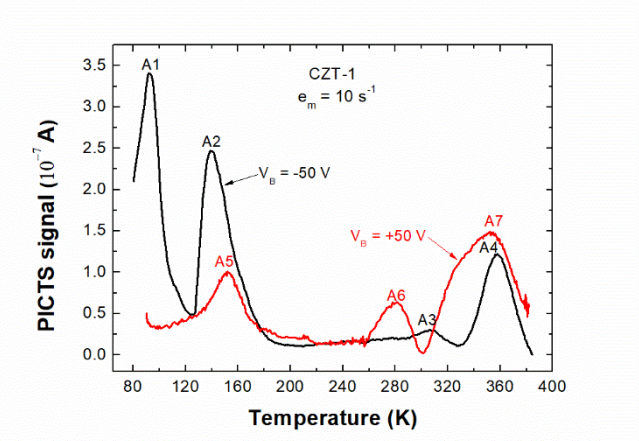

Fig. 1. PICTS spectra acquired at rate window e_m = 10 s^{-1} for the VB grown oxygen plasma treated CZT-1 sample under two different bias conditions V_B = -50 V and +50 V.

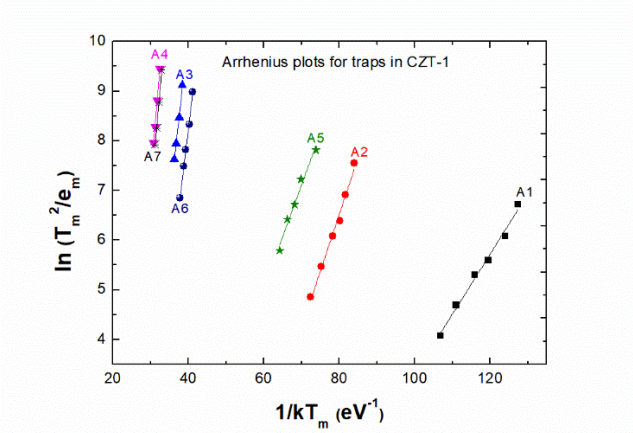

Fig. 2. Arrhenius plots of $\ln(T_m^2/e_m)$ versus $1/kT_m$ for the peaks A1-A7 observed in the CZT-1 sample.

Figure 3(a) illustrates the TEES spectra obtained for the CZT-1 sample with two trap filling bias conditions: (1) V_B = -50 V applied to top contact during laser excitation at 80 K (i.e. higher possibility for populating electron traps) and (2) V_B = +50 V applied to DUT during illumination (i.e. condition for hole population). It is worth recalling that the TEES spectrum was acquired without any bias voltage during the thermal scan. Three distinct negative peaks at ~115 K, ~152 K and ~245 K are noticed in the TEES of Fig. 3(a). A single TEES/TSC peak, $I^{i}_{TSC}(T)$ resulting through thermal emission from a particular trap can be expressed in the first order kinetics approximation [34,37,41,67]:

$$I^{i}_{TSC}(T) = K_G \mu\tau N_{T,i} D_{t,i} T^2 \exp\left[-\frac{E_{T,i}}{kT} - \frac{kD_{T,i}T^4}{\beta E_{T,i}} e^{-E_{T,i}/kT} \times \left(1 - \frac{4kT}{E_{T,i}} + \frac{20k^2T^2}{E_{T,i}^2} \right) \right] \quad (2)$$

where $K_G = qAE$ is the geometrical factor, q is the elementary charge, A is the device active area, E is the electric field, $\mu\tau$ is the carrier mobility-lifetime product, N_T is the trap concentration, $D_{t,i} = 3\times10^{21}(m^*/m_0)\sigma_i$ is the trap dependent coefficient, m_0 is the electron rest mass, the effective mass of electron and hole is $m_e^* = 0.14m_0$ and $m_h^* = 0.37m_0$ [41,44], and β is the heating rate. The sum of TSC peaks belonging to specific trap levels comprised with the dark current are represented by a temperature dependent fitting function called as simultaneous multiple peak analysis (SIMPA), $I_{SIMPA}(T)$ [34,37]

$$I_{SIMPA}(T) = \sum_{i=1}^{m} I^{i}_{TSC}(T) + I_{dark}(T) \quad (3)$$

$$I_{dark}(T) = Ce^{-E_{DD}/kT} \quad (4)$$

where C is the constant and E_{DD} is the deep-donor level controlling the dark current, $I_{dark}(T)$. In most cases, the trap signatures deduced from the PICTS are taken for SIMPA curve fitting Eqns. 2-4 (here $K_G \mu\tau N_T$ used as the fitting parameter) with the measured spectrum. In case, no matching is found between the TEES peak and PICTS results, the activation energy of the particular peak is estimated by assuming a reasonable capture cross-section of 10^{-15} cm^{-2} in the Eqn. 2. According to the 6517A Electrometer electrical connections used in the measurement setup, negative and positive peaks in the TEES spectra reveal electron and hole traps [78,80], respectively. From the SIMPA fitting, it is found that trap parameters of A2, A5 and A3 are related with the negative peaks at ~115 K and ~245 K. Accordingly, it is considered that the two electron traps A2 (E_C - 0.19 eV) and A5 (E_C - 0.24 eV) are merged and produced a broad negative peak at ~115 K; the negative peak at ~245 K is created by the electron trap A5 (E_C - 0.64 eV). Whereas the negative peak ~152 K are not correlated with the any of traps A1-A7 detected by PICTS. By considering $\sigma = 10^{-15}$ cm^{-2}, a new electron trap at A8 (E_C - 0.35 eV) is determined from the negative TEES peak seen around 152 K. For hole population condition (V_B = +50V), the same traps A2 and A5 are detected but with a weaker magnitude, confirming that these states are electron traps. The TSC spectrum measured under bias voltage V_B = -10 V for CZT-1 (electron

population case at T_0) is shown in Fig. 3(b), along with the steady-state thermal emission current (I_{dark}). The traps A2 and A5 are also perceived in Fig. 3(b) with the increased signal density; however, the trap A5 is not noticeable in the TSC spectrum due to the thermal generation current domination beyond 260K. Therefore, the TEES is more effective in identifying deep-level traps in the compensated CZT materials as compared to the TSC.

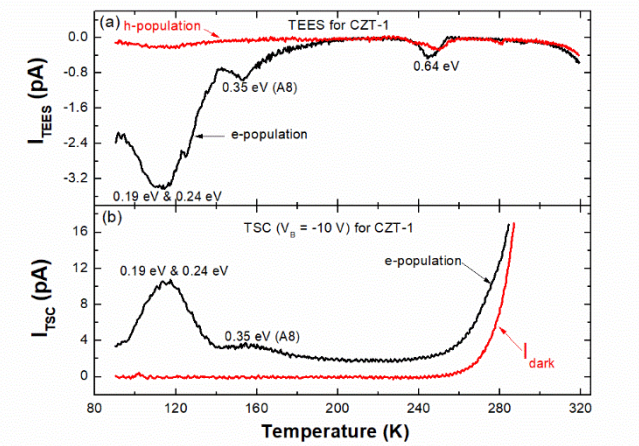

Fig. 3. (a) TEES for CZT-1 sample acquired with two trap filling bias conditions V_B = -50 V and +50 V at T_0. (b) TSC spectrum obtained under V_B = -10 V for CZT-1 (electron population at T_0) is shown along with the steady-state thermal emission dark current (I_{dark}).

The natural logarithm of steady-state thermal generation dark current for CZT-1 in the temperature range of 290-320 K is plotted in Fig. 4. The deep-donor energy (E_{DD} = 0.82 eV) is determined for the CZT-1 from the linear fit of $ln(I_{dark})$ versus $1/kT$ Arrhenius plot as per the Eqn. 4. The E_{DD} level (0.82eV) of CZT-1 is located near the middle of the bandgap, so it should control the Fermi level pinning position near the midgap through electrical compensation of native acceptors in the bulk [45,46], thereby achieving high-resistivity ($\rho > 10^9$ Ω cm) CZT crystals.

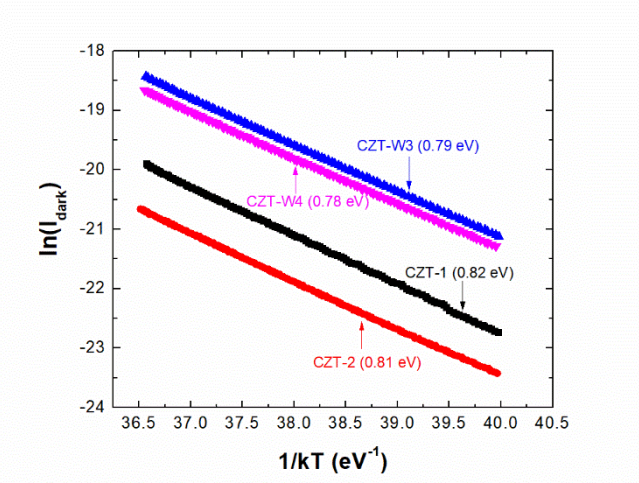

Fig. 4. Identification of deep-level donor energy (E_{DD}) for CZT-1, CZT-2, CZT-W3, and CZT-W4 crystals by the linear fits of $ln(I_{dark})$ versus $1/kT$ Arrhenius plots.

The PICTS spectra in Fig. 5 for the VB grown CZT-2 sample reveal three traps B1 (0.11±0.01 eV, 4×10^{-20} cm^{-2}), B2 (0.64±0.03 eV, 2.7×10^{-14}), B3 (0.86±0.02 eV, 5.6×10^{-13}) under negative bias voltage V_B = -50 V; and two traps B4 (0.11±0.01 eV, 2×10^{-20} cm^{-2}), B5 (0.61±0.02, 3.6×10^{-14}) at V_B = +50 V. The PICTS at +50 V was not measurable beyond 340 K due to the rapid rise in the dark current, so the trap at 0.85 eV is not detected for the positive bias voltage. The TEES of CZT-2 samples obtained with electron and hole population conditions is plotted in Fig. 6(a). The electron trap emitting around 265 K is associated with the defect B2 (E_C - 0.65 eV). The negative peaks at ~115K and ~152K are related to the traps A5 (E_C - 0.24 eV) and A8 (E_C - 0.35 eV) detected in CZT-1. In the hole-population case, only a small negative peak is seen at ~260 K and other two peaks are absent, which confirms that these defect states are electron traps. The occurrence of these three traps (E_C - 0.24 eV, E_C - 0.35 eV, E_C - 0.65 eV) in the TSC spectrum of CZT-2 further support the TEES results, as perceived from Fig. 6(b). The E_{DD} = 0.81 eV is determined for CZT-2 by the linear fit of $ln(I_{dark})$-$1/kT$ plot shown in Fig. 4.

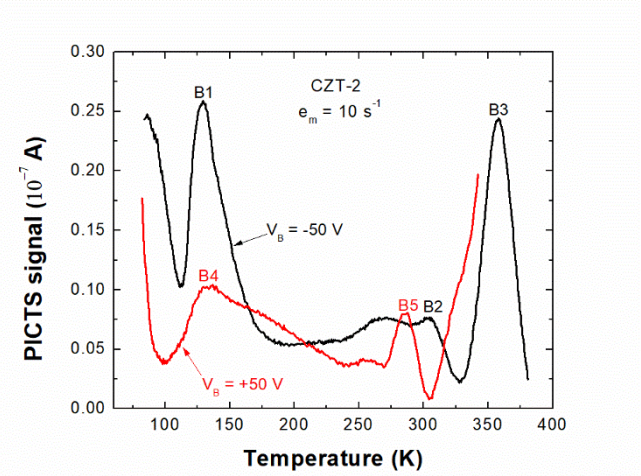

Fig. 5. PICTS (e_m = 10 s^{-1}) for the VB grown oxygen plasma treated CZT-2 sample under two different bias voltages V_B = -50 V (preferential electron injection) and +50 V (preferential hole injection).

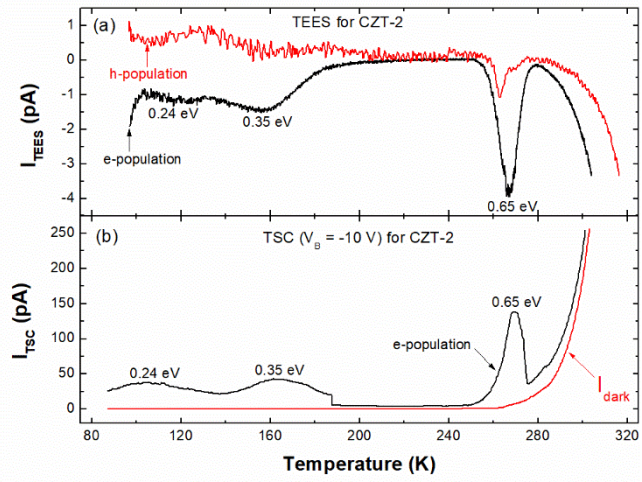

Fig. 6. (a) TEES for CZT-2 sample attained with electron and hole population conditions. (b) TSC spectrum at V_B = -10 V and I_{dark} spectrum for CZT-2.

Figure 7 shows the photoconductivity current characteristics of the CZT-1 and CZT-2 samples obtained using 650 nm illumination. The subtraction of the dark current from the photocurrent yields the photoconductivity current. The effective carrier mobility-lifetime (μτ) product can be estimated by fitting the photoconductivity current with the modified Hecht equation under the assumptions of a uniform electric field and no carrier de-trapping in the DUT [29,65,72-75]:

$$I(V_B) = \frac{I_0 \mu\tau V_B}{L^2}\left(1 - e^{-\frac{L^2}{\mu\tau V_B}}\right)\frac{1}{1+\frac{L}{V_B}\frac{s}{\mu}} \qquad (5)$$

where $I(V_B)$ is the photocurrent at the bias voltage V_B, I_0 is the saturation photocurrent, L is the sample thickness, and s is the surface recombination velocity. The effective μτ product for CZT-1 and CZT-2 samples is calculated as 3.2×10^{-4} cm^2/V, and 4×10^{-4} cm^2/V from the Hecht fitting with negligible surface recombination velocity. Thus, quite similar μτ product values are estimated for the CZT-1 and CZT-2 crystals. The μτ product of the CZT crystals can be further improved by the sub-bandgap illumination [29].

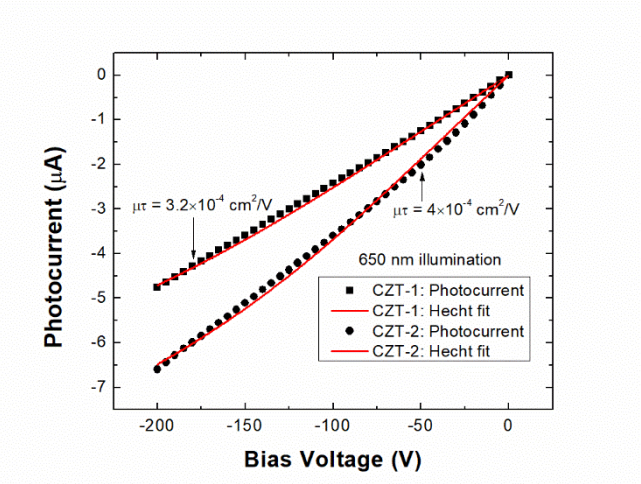

Fig. 7. The photoconductivity current characteristics obtained using 650 nm illumination for the CZT-1 and CZT-2 samples are fitted with the Hecht equation.

The deep-level defects identified in the VB grown CZT-1 and CZT-2 samples are summarized in Table 1. The traps are grouped based on their activation energy, capture cross-section and peak position in PICTS. The trap signatures and peak positions for the peaks B1 and B4 are quite similar, so it is considered that these peaks are produced by the same trap (denoted as X1). Similarly, the peaks A6 and B5 are grouped as an identical trap X6; A3 and B2 are categorized as X6; the peaks A4, A7 and B3 are grouped as X8. Several defects are common and nearly the same μτ product values are identified in CZT-1 and CZT-2 samples, which indicates that these CZT crystals have identical crystalline quality. Overall, eight distinct trap levels (X1-X8) are observed in the VB grown CZT-1 and CZT-2 crystals.

The traps in the CZT-1 and CZT-2 are attributed to the defects reported in the literature according to their activation energy. The possible defects for the X1 (0.11 eV) and X2 (0.12 eV) traps are single

ionized Cd vacancies V_{Cd}^{-} [40,42,44,46,48], A-center defect complex composed of Cd-vacancy and In-dopant (V_{Cd}-In_{Cd}) [39,45,46], In-impurity related defect In_{Cd}^{+} [41], Cd-vacancy and Cl-impurity defect complex observed in CdTe [21]. The electron traps X3 (E_C - 0.19 eV) and X4 (E_C - 0.24 eV) are assigned to dislocation-related intrinsic defects [39,43], structural defects formed by Te-inclusion or precipitation [50], and the isoelectric oxygen-Cd vacancy pair $(O_{Te}\text{-}V_{Cd})^{-/2-}$ found in CdTe [70]. The microscopic origin for the electron trap at E_C - 0.35 eV (X5) is the doubled ionized Te antisite (Te_{Cd}^{++}) [50]. The deep-level trap X6 (0.61 eV) is ascribed to the Zn-related physical origin [22,37]. The deep electron states at E_C - 0.65 eV (X7) are associated with the doubly ionized Cd-interstitial (Cd_i^{++}) [21,68], Lead-related origin [43], and deep-level identified in the CZT single crystal by photo-hall effect spectroscopy (PHES) technique [56]. The deep-level defect X8 (0.85-0.86 eV) are assigned to the Te_{Cd} or V_{Cd} defect associated with an impurity [25], $(Te_{Cd}+V_{Cd})^{2-/-}$ defect complex [38], Ni-impurity induced deep-level states [27], and the deep electron trap determined from the time and temperature evolution of the electric field upon optical excitations [13]. Note that, the X8 is located near the E_{DD} (0.81-0.82 eV), so the trap X8 should also play a major role in controlling the bulk resistivity of CZT-1 and CZT-2 crystals.

The carrier de-trapping time (t_{dt}) of the defects is calculated at 300 K based on the following equation and is given in Table 1 [68,81]:

$$t_{dt} = \frac{1}{N_C v_{th} \sigma} \exp\left(\frac{-E_T}{kT}\right) \quad (6)$$

The carrier de-trapping time increases with the increasing activation energy, as noted from Table 1. Although X1 (0.11 eV) is a shallow trap, the de-trapping time of X1 (7.5×10^{-5} - 1.5×10^{-4} s) is higher than that for intermediate trap X5 (0.35 eV, $t_{dt} = 3.3\times10^{-6}$ s) due to the lower capture cross-section of X1. Hence, the carrier emission rate depends not only on the energy position, but also their capture cross-section. Significantly longer de-trapping times (> 0.02 s) are noticed for E_T > 0.6 eV. The emission time constant of the deep-level defect X8 is found to be 16-23 s. The carrier trapping time (t_t) of defect $t_t \sim [N_T v_{th} \sigma]^{-1}$. $[1+10^6 \cosh (E_T\text{-}E_i)/kT]$ dictates that the deep-level traps are faster in capturing the charge carries than the swallow levels [27-29]. The deep-level defects have faster capture time and slower emission rate. This implies that the deep-level traps can quickly capture the excess charge carriers introduced in the detectors, but the de-trapping process is much slower such that may exceed the data acquisition time of the detector read-out electronics [27-29]. Therefore, the deep-level traps (E_T > 0.6 eV) are mainly responsible for incomplete charge collection and $\mu\tau$ product degradation in the CZT radiation detectors.

Table 1. Deep-level defects identified in VB-grown CZT-1 and CZT-2 crystals by PICTS and TEES.

Label	Group	E_T (eV)	σ (cm^{-2})	t_{dt} at 300K (s)	Possible defects
B1,B4	X1	0.11	$(2\text{-}4)\times10^{-20}$	7.5×10^{-5} - 1.5×10^{-4}	V_{Cd}^{-} [40,42,44,46,48], V_{Cd}-In_{Cd} [39,45,46], In_{Cd}^{+} [41], V_{Cd}-Cl_{Te} [21]
A1	X2	0.12	3×10^{-17}	1.5×10^{-7}	
A2	X3	E_C - 0.19	1×10^{-17}	6.7×10^{-6}	dislocation related intrinsic defects [39,43], Structural defects [50], $(O_{Te}\text{-}V_{Cd})^{-/2-}$ [70]
A5	X4	E_C - 0.24	$(3\text{-}7)\times10^{-16}$	6.6×10^{-7} - 1.5×10^{-6}	
A8	X5	E_C - 0.35	1×10^{-15}	3.3×10^{-6}	Te_{Cd}^{++} [50]
A6, B5	X6	0.61	$(3\text{-}4)\times10^{-14}$	0.019 - 0.025	Zn-related origin [22,37]
A3, B2	X7	E_C - (0.64-0.65)	$(2\text{-}3)\times10^{-14}$	0.11 - 0.17	Cd_i^{2+} [21,68], Lead-related origin [43]
A4, A7, B3	X8	0.85-0.86	$(5\text{-}6)\times10^{-13}$	16 - 23	Te_{Cd} or V_{Cd} with impurity [25], $(Te_{Cd}+V_{Cd})^{2-/-}$ [38], Ni-related [27]
E_{DD}		0.81-0.82 V			

3.2. Traps in VB-ACRT grown CZT crystals

Figure 8 shows the PICTS spectra (e_m = 10 s^{-1}) acquired for VB-ACRT grown CZT-W3 sample under negative (V_B = -50V) and positive (V_B = +50V) bias voltages. From the Arrhenius analysis, four traps are identified at V_B = -50 V: C1 (0.23±0.01 eV, 10^{-17} cm^{-2}), C2 (0.34±0.02 eV, 10^{-15} cm^{-2}), C3 (0.42±0.03 eV, 10^{-16} cm^{-2}), and C4 (0.82±0.04 eV, 4×10^{-13} cm^{-2}); and three defects are detected under V_B = +50 V: C5 (0.23±0.01 eV, 4×10^{-17} cm^{-2}), C6 (0.34±0.02 eV, 5×10^{-16} cm^{-2}), and C7 (0.65±0.04 eV, 3.5×10^{-14} cm^{-2}). The TEES spectra attained with electron and hole population conditions for the CZT-W3 is depicted in Fig. 9(a). The negative peaks at ~148 K and ~197 K are consistent with the trap parameters of C2 (E_C - 0.34 eV) and C3 (E_C - 0.42 eV) according to the Eqn. 2. By choosing σ = 10^{-15} cm^{-2}, the energy level corresponding to the negative peak at ~212 K is estimated as E_C - 0.5 eV (i.e. new defect C8 detected in TEES). It is found that the hole trap C1 (E_V + 0.23 eV) produces the positive peak around 127 K in the TEES in Fig. 9(a) obtained for hole-population condition.

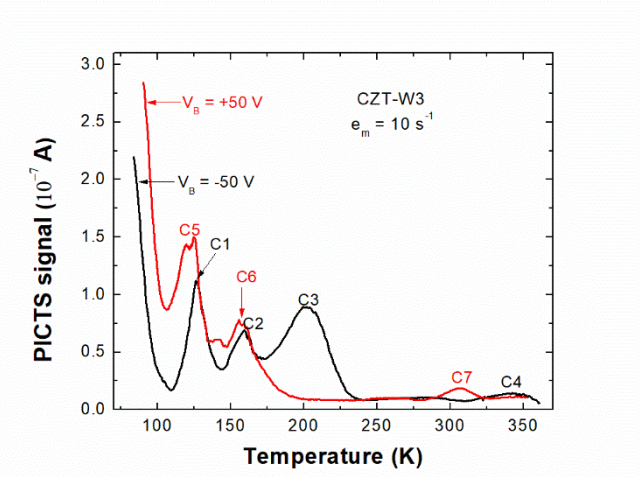

Fig. 8. PICTS (e_m = 10 s^{-1}) acquired for VB-ACRT grown CZT-W3 sample under negative (V_B = -50V) and positive (V_B = +50V) bias voltages.

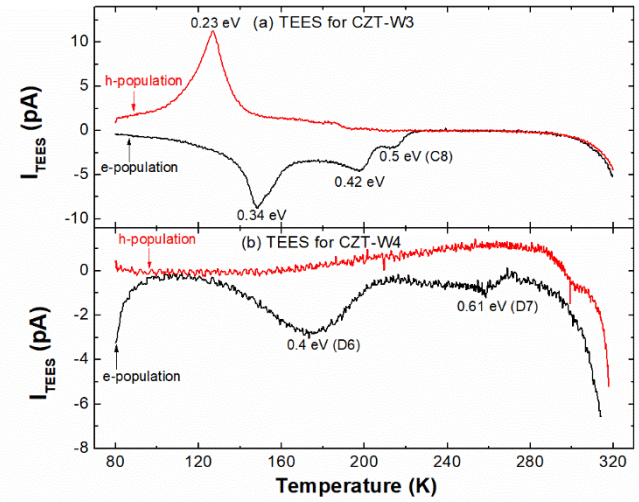

Fig. 9. TEES spectra attained with electron and hole population conditions for the VB-ACRT grown (a) CZT-W3 and (b) CZT-W4 crystals.

The PICTS spectra obtained at the rate window e_m = 35 s^{-1} for VB-ACRT grown CZT-W4 sample under V_B = -50V and +50V are shown in Fig. 10. The low temperature peak D1 is not clearly visible at the rate windows e_m = 10 s^{-1} and 20 s^{-1}. For better visualization of the peak D1, the PICTS acquired at e_m = 35 s^{-1} is depicted in Fig. 10. Four traps are observed from the PICTS under V_B = -50 V: D1 (0.12±0.01 eV, 6.5×10^{-17} cm^{-2}), D2 (0.16±0.01 eV, 10^{-15} cm^{-2}), D3 (0.28±0.01 eV, 9×10^{-17} cm^{-2}), and D4 (0.81±0.03 eV, 4.3×10^{-13} cm^{-2}). On the other hand, a single defect state D5 (0.78±0.04 eV, 9×10^{-14} cm^{-2}) is identified in the PICTS (Fig. 10) at V_B = +50V. Figure 9(b) displays the TEES spectra attained for the CZT-W4 sample with electron and hole population conditions. The negative peaks at ~175 K and ~255 K do not correspond to any of the defects observed in the CZT-W3. So, new trap levels D6 (E_C - 0.4 eV) and D7 (E_C - 0.61 eV) are detected from the TEES negative peaks at ~175 K and ~255 K by considering $\sigma = 10^{-15}$ in the TSC fitting Eqn. 2. While, no clear peaks are noticed in the TEES of Fig. 9(b) acquired with the hole-population condition. The deep-donor energy responsible for carrier compensation in the VB-ACRT grown CZT-W3 and CZT-W4 is determined as E_{DD} = 0.78-0.79 eV by the linear fit of the $ln(I_{dark})$-$1/kT$ plot shown in Fig. 4. The effective values of the μτ product for CZT-W3 (6×10^{-4} cm^2/V) and CZT-W4 (7.3×10^{-4} cm^2/V) samples are estimated by fitting the measured photocurrent properties with the modified Hecht equation, as plotted in Fig. 11. So, the μτ for CZT-W3 is slightly lower than the CZT-W4, may be due to the presence of the deep-level traps at E_C-0.5 eV (Y7) and 0.65 eV (Y9) in the CZT-W3. However, these μτ values are notably higher than that for the CZT-1 and CZT-2 samples.

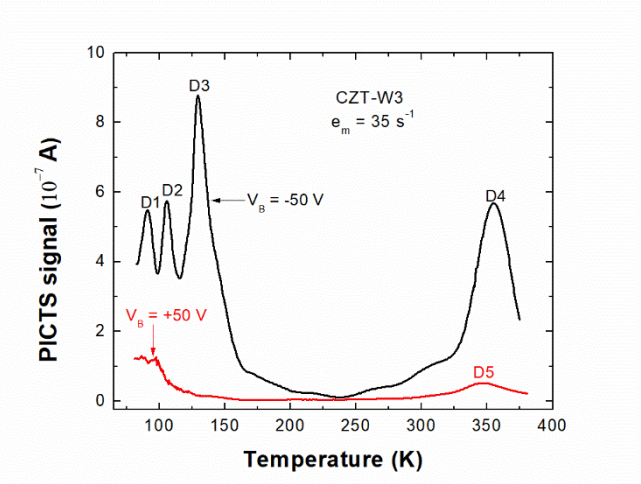

Fig. 10. PICTS obtained at the rate window e_m = 35 s^{-1} for VB-ACRT grown CZT-W4 sample under positive (V_B = -50V) and negative (V_B = +50V) voltages.

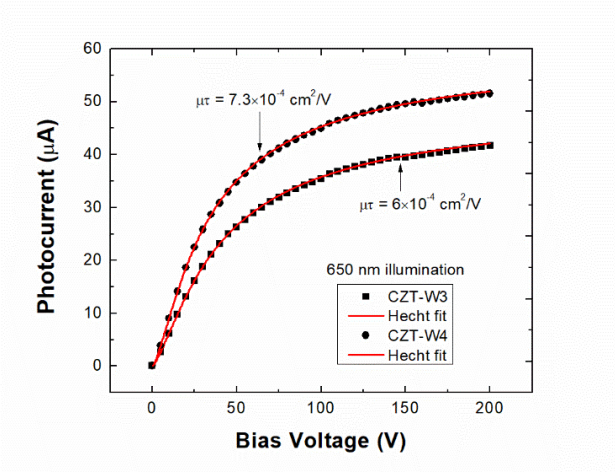

Fig. 11. The effective values of the μτ product for CZT-W3 (6×10^{-4} cm^2/V) and CZT-W4 (7.3×10^{-4} cm^2/V) samples are estimated by fitting the measured photocurrent properties with the modified Hecht equation.

The deep-level traps present in the VB-ACRT grown CZT-W3 and CZT-W4 crystals are summarized in Table 2, together with computed (using Eqn. 5) carrier de-trapping time (t_{dr}) of the defects. The defects are grouped based on their activation energy, capture cross-section and peak position in the PICTS: C1 and C5 are assigned under Y3; C2 and C5 are classified as Y5; C3 and D6 are categorized as Y6; C4 and D4 are grouped as Y11. The swallow trap Y1 (0.12) are attributed to the V_{Cd}^- [40,42,44,46,48], V_{Cd}-In_{Cd} [39,45,46], In_{Cd}^+ [41], and V_{Cd}-Cl_{Te} [21]. The trap Y2 (0.16) is also assigned to the A-center defect (V_{Cd} - In_{Cd}) complex [20,28,34,53]. The possible defects for the hole trap at E_V+0.23 eV (Y3) are Zn-related defect [34], doubly ionized Cd-vacancy (V_{Cd}^{2-}) [54], and V_{Cd} or related defect complex [51]. The microscopic origins for the trap Y4 (0.28 eV) are structural defects [36,37] and In-related defect [43,49,53]. The doubled ionized Te_{Cd}^{++} [50] may produce the electron trap at E_C - 0.35 eV (Y5). The electron trap at E_C - (0.4-0.42) eV (Y6) may correspond to the Te_{Cd}-associated defect [36], Ga-related defect complex [43], Cu-impurity induced complex acceptor [43], and V_{Cd}-related deep-donor [55]. The electron trap at E_C - 0.5 eV (Y7) may be attributed to the residual impurities in the In-doped CdTe [43] and Cl-related defect [49]. The defect Y8 (E_C -0.61 eV) may be associated

with the Zn cation vacancy (Zn-related origin) [22,37]. The probable physical origins for the defect Y9 (0.65 eV) are the Cd-interstitial (Cd_i^{++}) [21,68], Te-interstitials (Te_i^{2-}) [42], and Lead-related level [43]. The deep-level defect Y10 (0.78 eV) are related to the V_{Cd}^{-} induced deep acceptors [20], acceptor defect complex comprised of V_{Cd} and an impurity [21], Cl-associated A-center (V_{Cd}-Cl_{Te}) defect complex [21], second ionized state of Cd-vacancy (V_{Cd}^{2-}) [13], and Te_{Cd} related deep donor [11,23]. The deep-level trap Y11 (0.81-0.82 eV) are ascribed to the Te_{Cd} or V_{Cd} defect with an impurity [25], $(Te_{Cd}+V_{Cd})^{2-/-}$ [38], the deep-level identified in CZT crystal by the photo-hall effect spectroscopy (PHES) [56]. The deep-level defects such as Y10 (0.78 eV), Y11 (0.81-0.82 eV) and deep-donor level (0.78-0.79 eV) are located near to each other. Hence, in addition to E_{DD}, the mid-gap states Y10 and Y11 should also participate in the carrier compensation in the CZT-W3 and CZT-W4 substrates.

The activation energies of the traps Y1 (0.12 eV), Y5 (E_C - 0.34 eV), Y8 (E_C - 0.61 eV), Y9 (0.65 eV), Y11 (0.81-0.82 eV) are quite consistent with the defects X1 (0.11 eV) and X2 (0.12 eV), X5 (E_C - 0.35 eV), X6 (0.61 eV), X7 (E_C - 0.65 eV), X8 (0.85-0.86 eV) observed in VB-grown CZT crystals. The Te-inclusion induced structural defects X3 (E_C - 0.19 eV) and X4 (E_C - 0.24 eV) are not detected in the VB-ACRT grown CZT crystals. On the other hand, five new defects Y2 (0.16 eV), Y3 (E_V + 0.23 eV), Y4 (0.28 eV), Y6 (E_C -0.4 eV), Y10 (0.78 eV) are identified in the VB-ACRT grown CZT-W3 and CZT-W4 crystals. The de-trapping time for the swallow trap Y1 and deep-level trap Y8 at 300K is computed as 6.9×10^{-8} s and 0.75 s, respectively. So, longer emission time constants (> 0.75 s) are estimated for the deeper energy states (E_T > 0.6 eV) at 300 K. This reveals that the deep-level traps (Y8, Y9, Y10, and Y11) are the major detrimental defects affecting the carrier mobility-lifetime product in the VB-ACRT grown CZT-W3 and CZT-W4 crystals.

Table 2. Deep-level traps in VB-ACRT grown CZT-W3 and CZT-W4 deduced from PICTS and TEES.

Label	**Group**	**E_T (eV)**	**σ (cm^2)**	**t_{dt} at 300K (s)**	**Possible defects**
D1	Y1	0.12	6.5×10^{-17}	6.9×10^{-8}	V_{Cd}^{-} [40,42,44,46,48], V_{Cd}-In_{Cd} [39,45,46], In_{Cd}^{+} [41], V_{Cd}-Cl_{Te} [21]
D2	Y2	0.16	10^{-15}	2.1×10^{-8}	A-center (V_{Cd} - In_{Cd}) [20,28,34,53]
C1, C5	Y3	E_V + 0.23	$(1\text{-}4)\times10^{-17}$	7.9×10^{-6} - 3.2×10^{-5}	Zn-related [34], V_{Cd}^{2-} [54], V_{Cd} or related defect complex [51]
D3	Y4	0.28	9×10^{-17}	2.4×10^{-5}	Structural defects [36,37], In-related [43,49,53]
C2, C6	Y5	E_C - 0.34	$(0.5\text{-}1)\times10^{-15}$	2.2×10^{-5} - 4.4×10^{-5}	Te_{Cd}^{++} [50]
C3, D6	Y6	E_C - (0.4-0.42)	10^{-15} - 10^{-16}	0.002 - 0.005	Te_{Cd} related [36], Ga-related complex [43], Cu-impurity [43], V_{Cd} related deep-donor [55]
C8	Y7	E_C - 0.5	10^{-15}	0.011	residual impurities in CdTe [43], Cl-related [49]
D7	Y8	E_C - 0.61	10^{-15}	0.75	Zn-related origin [22,37]
C7	Y9	0.65	3.5×10^{-14}	0.1	Cd_i^{2+} [21,68], Te_i^{2-} [42], Lead-related origin [43]
D5	Y10	0.78	9×10^{-14}	6	Clorine A-center [21], V_{Cd}^{-} related [20,21], Te_{Cd} deep donor [11,23]
C4, D4	Y11	0.81-0.82	$(4\text{-}4.3)\times10^{-14}$	42 - 63	Te_{Cd} or V_{Cd} with impurity [25], $(Te_{Cd}+V_{Cd})^{2-/-}$ [38]
E_{DD}		0.78-0.79 eV			

3.3. Traps in VB grown CMT crystals

Figure 12 displays the PICTS acquired at rate window e_m = 50 s^{-1} for VB grown CMT-1 sample under negative (V_B = -50 V) and positive (V_B = +50 V) bias voltages. The PICTS at e_m = 50 s^{-1} is plotted in Fig. 11 for the clear visualization of the low temperature peak E1. Eight traps are identified from the Arrhenius analysis of the PICTS peaks: E1 (0.11±0.01 eV, 2×10^{-17} cm^{-2}), E2 (0.22±0.01 eV, 5×10^{-17} cm^{-2}), E3 (0.37±0.01 eV, 1.3×10^{-16} cm^{-2}), E4 (0.7±0.01 eV, 2×10^{-14} cm^{-2}), E5 (0.83±0.04 eV, 3×10^{-13} cm^{-2}) under V_B = -50 V; and E6 (0.14±0.02 eV, 10^{-19} cm^{-2}), E7 (0.36±0.03 eV, 4×10^{-16} cm^{-2}), E8 (0.68±0.04 eV, 2×10^{-14} cm^{-2}) under V_B = +50 V. The TEES spectra obtained for VB-grown CMT-1 with electron and hole population conditions are illustrated in Fig. 13. The negative peaks at ~160K, ~260K and ~270K are related to the defects E3 (E_C - 0.36 eV), E8 (E_C - 0.68 eV) and E4 (E_C - 0.7 eV) using the curve fitting analysis. The positive peak seen around 135 K in the hole-population case corresponds to the defect state E2 (E_V + 0.22 eV).

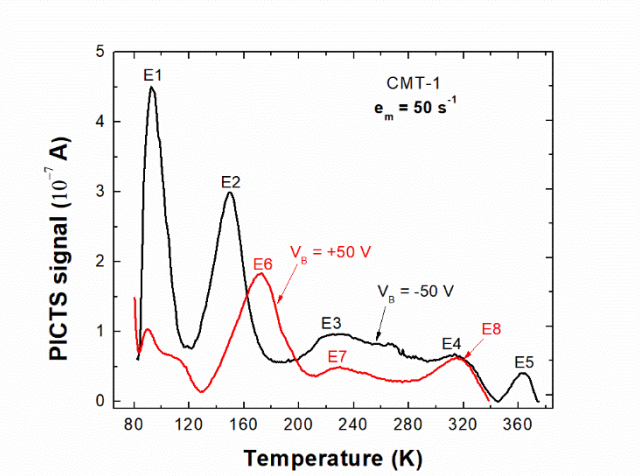

Fig. 12. PICTS acquired at rate window e_m = 50 s^{-1} for VB grown CMT-1 sample under negative (V_B = -50V) and positive (V_B = +50V) bias voltages.

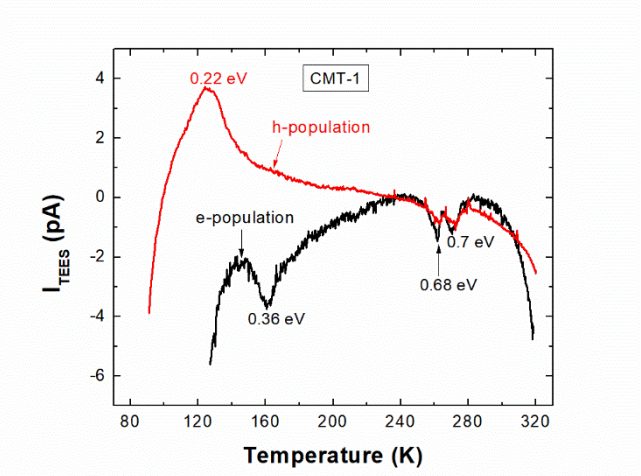

Fig. 13. TEES spectra obtained for VB-grown CMT-1 with electron and hole population conditions at T_0.

The PICTS spectra in Fig. 14 for CMT-2 crystal under V_B = -50 V reveal three electronic trapping centers such as F1 (0.22±0.01 eV, 7×10^{-16} cm^{-2}), F2 (0.48±0.02 eV, 3.5×10^{-12} cm^{-2}) and F3 (0.84±0.04 eV, 7×10^{-13} cm^{-2}). While a single trap F4 (0.13±0.01 eV, 2×10^{-16} cm^{-2}) is detected from the PICTS acquired under the positive bias voltage (V_B = +50 V). The strong negative peak at ~210 K in the TEES spectrum of CMT-2 (see Fig. 15) is produced most likely due to the electron trap F2 (E_C - 0.5 eV). The activation energy for the negative TEES peaks at ~250 K and ~270 K is estimated as E_C - 0.6 eV (F5) and E_C - 0.65 eV (F6) by considering $\sigma = 10^{-15}$ cm^{-2}. So, two new defect levels F5 and F6 are identified from the TEES of CMT-2 sample.

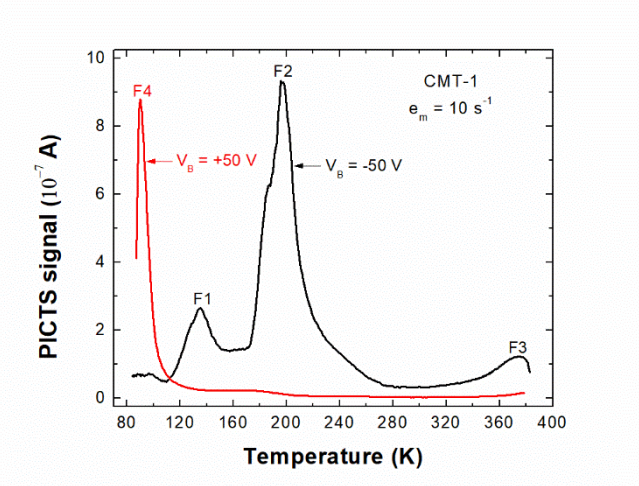

Fig. 14. PICTS acquired at the rate window e_m = 10 s^{-1} for CMT-2 crystal under V_B = -50 V and +50 V.

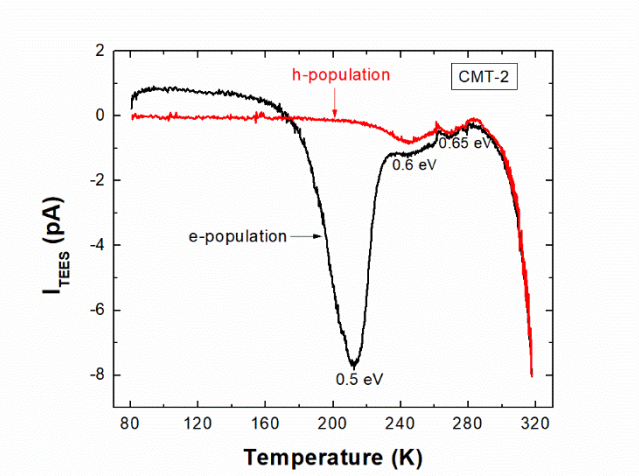

Fig. 15. TEES spectra obtained for CMT-2 with electron and hole population cases at T_0.

The PICTS spectra at e_m = 10 s^{-1} for the CMT-3 sample under V_B = -50 V are depicted in Fig. 16. For the better visualization of the low-temperature peak F1, the PICTS acquired at e_m = 100 s^{-1} with the same bias polarity is shown in the inset of Fig. 16. The PICTS at -50 V reveals four trap signatures: G1 (0.08±0.01 eV, 1.3×10^{-19} cm^{-2}), G2 (0.28±0.01 eV, 1.6×10^{-15} cm^{-2}), G3 (0.32±0.02 eV, 1.5×10^{-16} cm^{-2}) and G4 (0.84±0.04 eV, 7×10^{-13} cm^{-2}). Whereas no traps are found from the PICTS attained under the

positive voltage (V_B = + 50V). The TEES spectra for the CMT-3 for the electron and hole-population cases are shown in Fig. 17. The negative peak at ~145 K is associated with the electron trap G3 (E_C - 0.32 eV). The trap parameters for the negative peak around 190 K are calculated as G5 (E_C - 0.45 eV, 10^{-15} cm^{-2}). Figure 18 shows the $ln(I_{dark})$ versus $1/kT$ plots obtained from the dark current characteristics for the CMT-1, CMT-2 and CMT-3 crystals. The deep-donor energy responsible for carrier compensation in the CMT-1, CMT-2 and CMT-3 crystals are found to be 0.83 eV, 0.81 eV and 0.83eV, respectively. Furthermore, μτ product values for the CMT-1 (3.6×10^{-4} cm^2/V), CMT-2 (2.5×10^{-4} cm^2/V) and CMT-3 (2.5×10^{-4} cm^2/V) are calculated from DC photoconductivity properties shown in Fig. 19.

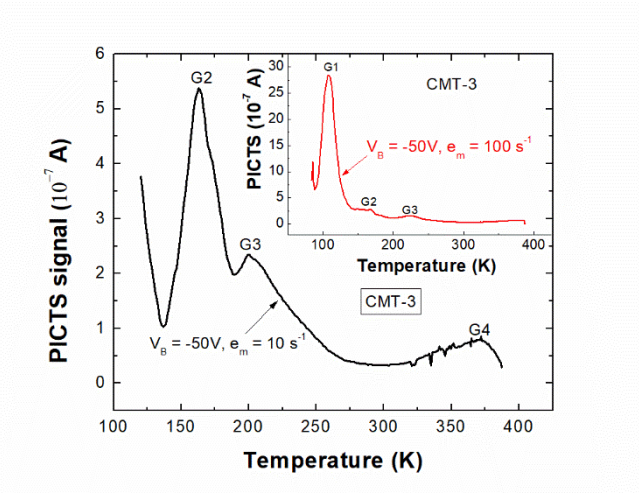

Fig. 16. PICTS acquired for CMT-3 crystal under V_B = -50 V at the rate window e_m = 10 s^{-1}. The inset shows the PICTS of CMT-3 for same bias polarity (V_B = -50 V), but at the different rate window e_m = 10 s^{-1}.

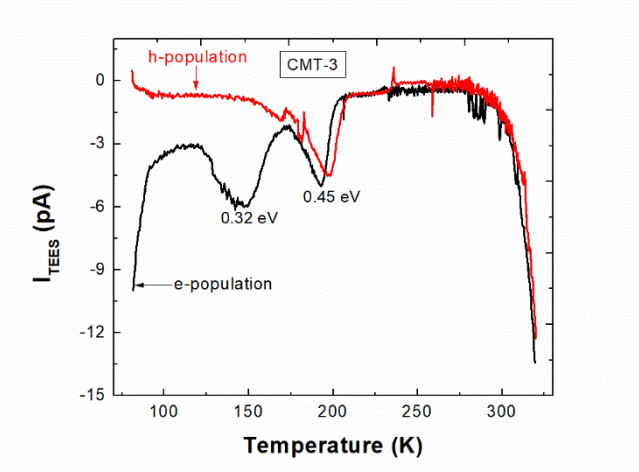

Fig. 17. TEES spectra attained for CMT-3 crystal under electron and hole population conditions at T_0.

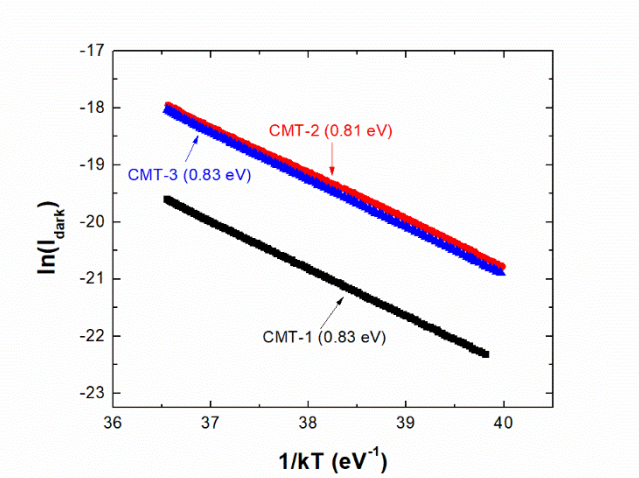

Fig. 18. Estimation of deep-level donor energy (E_{DD}) for CMT-1, CMT-2 and CMT-3 samples by the linear fits of $ln(I_{dark})$ versus $1/kT$ Arrhenius plots.

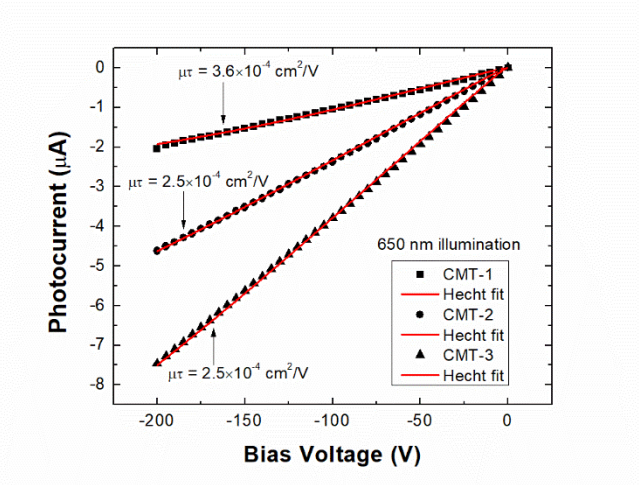

Fig. 19. The effective μτ product values for CMT-1 (3×10^{-4} cm^2/V), CMT-2 (2.5×10^{-4} cm^2/V) and CMT-3 (2.5×10^{-4} cm^2/V) samples are estimated by fitting the measured photocurrent with the Hecht equation.

The deep-level traps observed in the VB-grown CMT-1, CMT-2 and CMT-3 samples are summarized in Table 3. Based on the activation energy and capture cross-section, the E3 and E7 are grouped to an identical trap state Z9 and similarly the traps E5, F3 and G4 are categorized as Z14. The swallow level Z1 (0.08) corresponds to Cd-vacancy induced donor-type defects (V_{Cd}^{+}) [67] observed in the V-doped CMT crystals. The swallow trap Z2 (0.11 eV) may be produced due to the In-doping impurity [57]. The defect Z3 (0.13 eV) is assigned to the single ionized Cd-vacancy (V_{Cd}^{-}) [43,46] observed in the CZT crystals. The trap Z4 (0.14 eV) may be related to the electron trap detected in Ga-doped $C_{0.99}Mn_{0.01}T$ crystals [58] and the dislocations-induced defects [67] found in the V-doped CMT. The hole trap at E_V + 0.22 eV (Z5) are identified for the first time in CMT crystals, thus this hole trap may be attributed to the Mn-related origin. The possible defects for the trap Z6 (0.22 eV) are the V_{Cd}^{2-} [54], V_{Cd} or related defect complex [51] detected in the CZT. The energy position of the trap Z8 (0.28 eV) is nearly matched with the V-related [67] and X-level [67] defects identified in the V-doped CMT. Szatkowski et al. [57,59] also determined similar trap activation energies (~0.28 eV) in the Ga-doped

and In-doped CMT crystals. The possible defects for the electron trap at E_C - 0.32 eV (Z8) are the Te_{Cd} complex [67] and the electron trap detected in Ga-doped $C_{0.99}Mn_{0.01}T$ [58]. The microscopic origins for the electron trap Z9 at E_C - (0.35-0.36) eV are the Te_{Cd}^{++} [50], Te_{Cd}-$2V_{Cd}$ [67], and defect states found in the Ga-doped CMT [58]. The electron trap at E_C - 0.45 eV (Z10) are ascribed to the V_{Cd}-related defects [67], and acceptor-type $[Te_{Cd}\text{-}2V_{Cd}]^{2/-}$ [67]. The defect Z11 (0.48 eV) is also identified in the In-doped $Cd_{0.8}Mn_{0.2}Te$ [59] and $Cd_{0.85}Mn_{0.15}Te$ [62] crystals, which is attributed to the Cd-vacancy induced acceptor-states [65]. The closely located electron traps such as E_C - 0.68 eV (Z13) and E_C - 0.7 eV (Z14) are identified for the first time in the CMT, so these electron traps may be assigned to the Mn-related origins. The probable defects for the deep-level trap Z14 (0.83-0.84 eV) are the Te_{Cd} or V_{Cd} with impurity [25], $(Te_{Cd}+V_{Cd})^{2-/-}$ [38] defects determined in the CZT; this deep-level defects should play a major role in the electrical compensation in the CMT crystals, together with the deep-level donors located at 0.81-0.83 eV. The emission time constant of the defects is found to increase with the increasing trap energy (refer Table 3). The de-trapping time for the defects Z12, Z13, and Z14 are estimated as 1.13 s, 1.2-1.4 s, and 12.4-18.2 s, respectively. It is anticipated that the deep-level defects Z12-Z14 (E_T > 0.6 eV) should have faster capture time and slower emission rate. As a result, it is considered that the deep-level traps Z12 (E_C - 0.68 eV), Z13 (E_C - 0.7 eV), and Z14 (0.83-0.84 eV) are the major performance limiting defects present in the CMT crystal. From the Tables 1-3, it is noted that the activation energy of the traps Z1-Z4, Z6-Z11 and Z14 quite matches with the some of the defects observed in the CZT crystals. To the best of our knowledge, the hole trap at E_V + 0.22 (Z5) is not yet reported in the literature for the CMT crystals. Moreover, the electron traps at E_C - 0.68 eV (Z13) and E_C - 0.7 eV (Z14) are detected in the CMT for the first time, thereby these defects are attributed to the Mn-related microscopic origins.

Table 3. Deep-level traps observed in VB grown CMT-1, CMT-2 and CMT-3 crystals from PICTS and TEES.

Label	**Group**	**E_T (eV)**	**σ (cm^{-2})**	**t_{dt} at 300K (s)**	**Possible defects**
G1	Z1	0.08	1.3×10^{-19}	7.4×10^{-6}	V_{Cd}^{+} [67]
E1	Z2	0.11	2×10^{-17}	1.5×10^{-7}	In_{Cd}^{+} [57]
F4	Z3	0.13	2×10^{-16}	3.3×10^{-8}	V_{Cd}^{-} [43,46]
E6	Z4	0.14	10^{-19}	9.7×10^{-5}	dislocation-related [67]
E2	Z5	E_V + 0.22*	5×10^{-17}	4.3×10^{-6}	Mn-related
F1	Z6	0.22	7×10^{-16}	3×10^{-7}	V_{Cd}^{2-} [54], V_{Cd} or related defect complex [51]
G2	Z7	0.28	1.6×10^{-15}	1.4×10^{-6}	V-related [67], X-level [67]
G3	Z8	E_C - 0.32	1.5×10^{-16}	6.8×10^{-5}	Te_{Cd} complex [67]
E3, E7	Z9	E_C - (0.36-0.37)	$(1\text{-}4)\times10^{-16}$	$(4\text{-}7)\times10^{-4}$	Te_{Cd}^{++} [50], Te_{Cd}-$2V_{Cd}$ [67]
G5	Z10	E_C - 0.45	10^{-15}	0.002	V_{Cd}-related defects [67], $[Te_{Cd}\text{-}2V_{Cd}]^{2/-}$ [67]
F2	Z11	0.48	3.5×10^{-12}	1.4×10^{-6}	V_{Cd} acceptor [65]
E7	Z12	E_C - 0.68*	10^{-14}	1.13	Mn-related
E4	Z13	E_C - 0.7*	$(1\text{-}2)\times10^{-14}$	1.2 - 2.4	Mn-related
E5, F3, G4	Z14	0.83-0.84	$(3\text{-}7)\times10^{-13}$	12.4 - 18.2	Te_{Cd} or V_{Cd} with impurity [25], $(Te_{Cd}+V_{Cd})^{2-/-}$ [38]
E_{DD}		0.81-0.83 eV			

*these defects are reported for the first time in CMT crystals.

4. Conclusions

The deep-level defects in the CZT and CMT crystals are identified by the PICTS and TEES techniques. Eight distinct trap levels (X1-X8) are reported in the energy range of 0.11-0.86 eV for the VB grown CZT-1 and CZT-2 crystals. Several common defects (X1, X5, X6, X7 and X8) and nearly the same $\mu\tau$ product values are identified for CZT-1 (3.2×10^{-4} cm^2/V) and CZT-2 (4×10^{-4} cm^2/V) samples, thus these CZT crystals have identical crystalline quality. The deep-level trap X8 (0.85-0.86 eV) is located near the deep-donor energy (E_{DD} = 0.81-0.82 eV), thereby X8 should also play a major role in controlling the bulk resistivity of CZT-1 and CZT-2 crystals.

The PICTS and TEES measurements on the VB-ACRT grown CZT-W3 and CZT-W4 samples reveal eleven different traps (Y1-Y11) with the activation energies from 0.12 eV to 0.82 eV. In comparison with CZT-1 and CZT-2 samples, five new defects Y2 (0.16 eV), Y3 (E_V + 0.23 eV), Y4 (0.28 eV), Y6 (E_C -0.4 eV), Y10 (0.78 eV) are identified in the CZT-W3 and CZT-W4 crystals. The Te-inclusion induced structural defects X3 (E_C - 0.19 eV) and X4 (E_C - 0.24 eV) are not detected in the CZT-W3 and CZT-W4. In addition to E_{DD} = 0.78-0.79 eV, the mid-gap states Y10 and Y11 should also participate in the carrier compensation in the CZT-W3 and CZT-W4 substrates. The $\mu\tau$ product for CZT-W3 (6×10^{-4} cm^2/V) is slightly lower than the CZT-W4 (7.3×10^{-4} cm^2/V), may be due to the presence of the deep-level traps at E_C-0.5 eV (Y7) and 0.65 eV (Y9) in the CZT-W3. However, these $\mu\tau$ values are notably higher than that for the CZT-1 and CZT-2.

There are 14 distinct defects (Z1-Z14) are identified in the CMT-1, CMT-2 and CMT-3 crystals with the energy range of 0.08-0.84 eV. The deep-level defect X14 (0.83-0.84 eV) should play a major role in the electrical compensation in the CMT crystals, together with the deep-level donors located at 0.81-0.83 eV. The activation energy of the traps Z1-Z4, Z6-Z11 and Z14 quite matches with the some of the defects observed in the CZT crystals. To the best of our knowledge, the hole trap at E_V + 0.22 (Z5) and the electron traps at E_C - 0.68 eV (Z13) and E_C - 0.7 eV (Z14) are detected in the CMT for the first time, thereby these defects are attributed to the Mn-related microscopic origins.

It is anticipated that the deep-level defects (E_T > 0.6 eV) should have faster capture time and slower emission rate. As a result, it is considered that the deep-level traps viz. X6-X8, Y8-Y11, and Z12-Z14 are the major performance limiting defects affecting the charge collection properties of the CZT and CMT based radiation detectors.

Acknowledgement

Th authors would like to thank to Israeli branch of GE Healthcare and for supplying the crystals of CZT and CMT. We also like to thank Institute of Materials Research, Washington State University for providing CZT-W3 and CZT-W4 samples.

References

[1] T. E. Schlesinger, J. E. Toney, H. Yoon, E. Y. Lee, B. A. Brunett, L. Franks, R. B. James, Cadmium zinc telluride and its use as a nuclear radiation detector material, Mater. Sci. Eng. R Rep., 32 (2001) 103-189, doi: 10.1016/S0927-796X(01)00027-4.

[2] C. Szeles, CdZnTe and CdTe materials for X-ray and gamma ray radiation detector applications, Phys. Status Solidi Basic Res., 241 (2004) 783-790, doi: 10.1002/pssb.200304296.

[3] S. D. Sordo, L. Abbene, E. Caroli, A. M. Mancini, A. Zappettini, P. Ubertini, Progress in the development of CdTe and CdZnTe semiconductor radiation detectors for astrophysical and medical applications, Sensors, 9 (2009) 3491-3526, doi: 10.3390/s90503491.

[4] A. Brovko, A. Ruzin, Study of material uniformity in high-resistivity $Cd_{1-x}Zn_xTe$ and $Cd_{1-x}Mn_xTe$ crystals, Nucl. Instrum. Methods Phys. Res. A, 958 (2020) 161996, doi: doi.org/10.1016/j.nima.2019.03.051.

[5] A. Brovko, A. Adelberg, A. Ruzin, Effects of surface treatment on static characteristics of In/ $Cd_{1-x}Zn_xTe$/In and In/$Cd_{1-x}Mn_xTe$/In devices, Nucl. Instrum. Methods Phys. Res. A, 957 (2020) 163387, doi: 10.1016/j.nima.2020.163387.

[6] K. Kim, S. Cho, J. Suh, J. Hong, S. Kim, Gamma-ray response of semi-insulating CdMnTe crystals, IEEE Trans. Nucl. Sci., 56 (2009) 858-862, doi: 10.1109/TNS.2009.2015662.

[7] R. Rafiei, D. Boardman, A. Sarbutt, D. A. Prokopovich, K. Kim, M. I. Reinhard, A. E. Bolotnikov, R. B. James, Investigation of the charge collection efficiency of CdMnTe radiation detectors, IEEE Trans. Nucl. Sci., 59 (2012) 634-641, doi: 10.1109/TNS.2012.2190941.

[8] S. U. Egarievwe, W. Chan, K. H. Kim, U. N. Roy, V. Sams, A. Hossain, A. Kassu, R. B. James, Carbon coating and defects in CdZnTe and CdMnTe nuclear detectors, IEEE Trans. Nucl. Sci., 63 (2016) 236-245, doi: 10.1109/TNS.2016.2515108.

[9] Y. Du, W. Jie, T. Wang, Y. Xu, L. Yin, P. Yu, G. Zha, Vertical Bridgman growth and characterization of CdMnTe crystals for gamma-ray radiation detector, J. Cryst. Growth, 318 (2011) 1062-1066, doi: 10.1016/j.jcrysgro.2010.11.086.

[10] U. N. Roy, G. S. Camarda, Y. Cui, G. Gu, R. Gul, A. Hossain, G. Yang, S. U. Egarievwe, R. B. James, Growth and characterization of CdMnTe by the vertical Bridgman technique, J. Cryst. Growth, 437 (2016) 53-58, doi: 10.1016/j.jcrysgro.2015.12.017.

[11] X. Xing, J. Min, X. Liang, J. Zhang, L. Wang, L. Yang, Y. Ling, L. Duan, Y. Shen, Investigation of structural defects in In-doped CdZnTe under different in-situ annealing cooling rates, J. Cryst. Growth, 426 (2015) 270-275, doi: 10.1016/j.jcrysgro.2015.06.020.

[12] Y. Du, W. Jie, T. Wang, L. Luo, Y. Xu, L.Luan, Study on twin boundaries and Te particles in CdMnTe crystals for nuclear detector application, J. Cryst. Growth, 364 (2013) 128-132, doi: 10.1016/j.jcrysgro.2012.11.030.

[13] M. Rejhon, V. Dědič, L. Beran, U. N. Roy, J. Franc, R. B. James, Investigation of deep levels in CdZnTeSe crystal and their effect on the internal electric field of CdZnTeSe gamma-ray detector, IEEE Trans. Nucl. Sci., 66 (2019) 1952-1958, doi: 10.1109/TNS.2019.2925311.

[14] M. J. Mescher, T. E. Schlesinger, J. E. Toney, B. A. Brunett, R. B. James, Development of dry processing techniques for CdZnTe surface passivation, J. Electron. Mater., 28, (1999), 700-704, doi: 10.1007/s11664-999-0057-3.

[15] H. Chen, K. Chattopadhyay, K. -T. Chen, A. Burger, Passivation of CdZnTe surfaces by oxidation in low energy atomic oxygen, J. Vac. Sci. Technol. A, 17 (1999) 97-101, doi: 10.1116/1.581557.

[16] A. Brovko, O. Amzallag, A. Adelberg, L. Chernyak, P. V. Raja, A. Ruzin, Effect of oxygen plasma treatment on Cd1-xZnxTe material and devices, Nucl. Instrum. Methods Phys. Res. A (under review).

[17] A. Datta, S. Swain, Y. Cui, A. Burger, K. Lynn, Correlations of bridgman-grown $Cd_{0.9}Zn_{0.1}Te$ properties with different ampoule rotation schemes, J. Electron. Mater., 42 (2013) 3041-3053, doi: 10.1007/s11664-013-2782-x

[18] J. J. McCoy, S. Kakkireni, Z.H. Gilvey, S. K. Swain, A. E. Bolotnikov, K. G. Lynn, Overcoming mobility lifetime product limitations in vertical Bridgman production of cadmium zinc telluride detectors, J. Electron. Mater., 48, 7 (2019) 4226-4234, doi: 10.1007/s11664-019-07196-5.

[19] J. J. McCoy, S. Kakkireni, G. Gélinas, J. F. Garaffa, S. K. Swain, K. G. Lynn, Effects of excess Te on flux inclusion formation in the growth of cadmium zinc telluride when forced melt convection is applied, J. Cryst. Growth, 535 (2020) 125542, doi: 10.1016/j.jcrysgro.2020.125542.

[20] A. Castaldini, A. Cavallini, B. Fraboni, L. Polenta, P. Fernandez, J. Piqueras, Cathodoluminescence and photoinduced current spectroscopy studies of defects in $Cd_{0.8}Zn_{0.2}Te$, Phys. Rev. B, 54 (1996), 7622-7625, doi: 10.1103/PhysRevB.54.7622.

[21] A. Castaldini, A. Cavallini, B. Fraboni, P. Fernandez, J. Piqueras, Deep energy levels in CdTe and CdZnTe, J. Appl. Phys., 83 (1998) 2121-2126, doi: 10.1063/1.366946.

[22] A. Zumbiehl, P. Fougeres, M. Hage-Ali, J. M. Koebel, P. Siffert, A. Zerrai, K. Cherkaoui, G. Marrakchi, G. Bremond, Resistivity simulation of CZT materials, J. Cryst. Growth, 197 (1999) 670-674, doi: 10.1016/S0022-0248(98)00810-0.

[23] R. Gul, A. Bolotnikov, H. K. Kim, R. Rodriguez, K. Keeter, Z. Li, G. Gu, R. B. James, Point defects in CdZnTe crystals grown by different techniques, J. Electron. Mater., 40 (2011) 274-279, doi: 10.1007/s11664-010-1504-x.

[24] R. Gul et al., Point defects in Pb-, Bi-, and In-doped CdZnTe detectors: deep-level transient spectroscopy (DLTS) measurements, J. Electron. Mater., 41 (2012) 488-493, doi: 10.1007/s11664-011-1802-y.

[25] A. Cavallini, B. Fraboni, A. Castaldini, L. Marchini, N. Zambelli, G. Benassi, A. Zappettini, Defect characterization in fully encapsulated CdZnTe, IEEE Trans. Nucl. Sci., 60 (2013) 2870-2874, doi: 10.1109/TNS.2013.2270361.

[26] J. Suh, J. Hong, J. Franc, A. E. Bolotnikov, A. Hossain, R. B. James, K. Kim, Tellurium secondary-phase defects in CdZnTe and their association with the 1.1-eV deep trap, IEEE Trans. Nucl. Sci., 63 (2016) 2657-2661, doi: 10.1109/TNS.2016.2598743.

[27] R. Gul, U. N. Roy, R. B. James, An analysis of point defects induced by In, Al, Ni, and Sn dopants in Bridgman-grown CdZnTe detectors and their influence on trapping of charge carriers, J. Appl. Phys., 121 (2017) 115701, doi: 10.1063/1.4978377.

[28] R. Gul, U. N. Roy, G. S. Camarda, A. Hossain, G. Yang, P. Vanier, V. Lordi, J. Varley, R. B. James, A comparison of point defects in $Cd_{1-x}Zn_xTe_{1-y}Se_y$ crystals grown by Bridgman and traveling heater methods, J. Appl. Phys., 121 (2017) 125705, doi: 10.1063/1.4979012.

[29] J. Zhang et al., Effect of point defects trapping characteristics on mobility-lifetime ($\mu\tau$) product in CdZnTe crystals, J. Cryst. Growth, 519 (2019) 41-45, doi: 10.1016/j.jcrysgro.2019.04.026.

[30] Cs. Szeles, Y. Y. Shan, K. G. Lynn, E. E. Eissler, Deep electronic levels in high-pressure bridgman $Cd_{1-x}Zn_xTe$, Nucl. Instrum. Methods Phys. Res. A, 380 (1996) 148-152, doi: 10.1016/S0168-9002(96)00331-2.

[31] E. Y. Lee, R. B. James, R. W. Olsen, H. Hermon, Compensation and trapping in CdZnTe radiation detectors studied by thermoelectric emission spectroscopy, thermally stimulated conductivity, and current-voltage measurements, J. Electron. Mater., 28 (1999) 766-773, doi: 10.1007/s11664-999-0068-0.

[32] P. F. Wang, R. H. Nan, Z. Y. Jian, The relationship between deep-level defects and high resistivity characteristic in CdZnTe crystals, J. Mater. Sci.: Mater. Electron., 28, (2017) 5568-5573, doi: 10.1007/s10854-016-6223-5.

[33] R. Nan, T. Li, G. Xu, Z. Jian, X. Li, Distribution of microscopic defects in Al-doped CdZnTe crystal, J. Mater. Sci., 53 (2018) 4387-4394, doi: 10.1007/s10853-017-1895-7.

[34] M. Pavlović, M. Jakšić, H. Zorc, Z. Medunić, Identification of deep trap levels from thermally stimulated current spectra of semi-insulating CdZnTe detector material, J. Appl. Phys., 104 (2008) 023525, doi: 10.1063/1.2959354.

[35] Y. Xu, W. Jie, P. Sellin, T. Wang, W. Liu, G. Zha, P. Veeramani, C. Mills, Study on temperature dependent resistivity of indium-doped cadmium zinc telluride, J. Phys. D: Appl. Phys., 42 (2008) 035105, doi: 10.1088/0022-3727/42/3/035105.

[36] R. Nan, W. Jie, G. Zha, T. Wang, Y. Xu, W. Liu, Investigation on defect levels in CdZnTe: Al using thermally stimulated current spectroscopy, J. Phys. D: Appl. Phys., 43 (2010) 345104, doi: 10.1088/0022-3727/43/34/345104.

[37] R. H. Nan, W. Q. Jie, G. Q. Zha, X. X. Bai, W. Bei, Y. U. Hui, Determination of trap levels in CZT:In by thermally stimulated current spectroscopy, T. Nonferr. Metal. Soc., 22 (2012) s148-s152, doi: 10.1016/S1003-6326(12)61700-2.

[38] R. Soundararajan, K. G. Lynn, Effects of excess tellurium and growth parameters on the band gap defect levels in $Cd_xZn_{1-x}Te$, J. Appl. Phys., 112 (2012) 073111, doi: 10.1063/1.4757595.

[39] L. Xu, W. Jie, G. Zha, Y. Xu, X. Zhao, T. Feng, L. Luo, W. Zhang, R. Nan, T.Wang, Radiation damage on CdZnTe:In crystals under high dose ^{60}Co γ-rays, CrystEngComm, 15 (2013) 10304-10310, doi: 10.1039/c3ce41734d.

[40] L. Xu, W. Jie, X. Fu, G. Zha, T. Feng, R. Guo, T. Wang, Y. Xu, Y. Zaman, Effects of deep-level defects on carrier mobility in CdZnTe crystals, Nucl. Instrum. Methods Phys. Res. A, 767 (2014) 318-321, doi: 10.1016/j.nima.2014.08.040.

[41] L. Xu, W. Jie, X. Fu, A. E. Bolotnikov, R. B. James, T. Feng, G. Zha, T. Wang, Y. Xu, Y. Zaman, Axial distribution of deep-level defects in as-grown CdZnTe: In ingots and their effects on the material's electrical properties, J. Cryst. Growth, 409 (2015) 71-74, doi: 10.1016/j.jcrysgro.2014.09.039.

[42] R. Guo, W. Jie, N. Wang, G. Zha, Y. Xu, T. Wang, X. Fu, Influence of deep level defects on carrier lifetime in CdZnTe: In, J. Appl. Phys., 117 (2015) 094502, doi: 10.1063/1.4914159.

[43] Y. Zaman, W. Jie, T. Wang, L. Xu, Y. He, Y. Xu, G. Zha, R. Guo, X. Fu, Comparison of In doped and In, Pb co-doped $Cd_{0.9}Zn_{0.1}Te$, Nucl. Instrum. Methods Phys. Res. A, 790 (2015) 10-13, doi: 10.1016/j.nima.2015.04.014.

[44] L. Xu, W. Jie, B. Zhou, X. Fu, G. Zha, T. Wang, Y. Xu, T. Feng, X. Chen, Effects of crystal growth methods on deep-level defects and electrical properties of CdZnTe: In crystals, J. Electron. Mater., 44 (2015) 518-523, doi: 10.1007/s11664-014-3452-3.

[45] R. Nan, T. Wang, G. Xu, M. Zhu, W. Jie, Compensation processes in high-resistivity CdZnTe crystals doped with In/Al, J. Cryst. Growth, 451 (2016) 150-154, doi: 10.1016/j.jcrysgro.2016.07.032.

[46] Y. Gu et al., Correlated analysis of 2 MeV proton-induced radiation damage in CdZnTe crystals using photoluminescence and thermally stimulated current techniques, Nucl. Instrum. Methods Phys. Res. B, 386 (2016) 16-21, doi: 10.1016/j.nimb.2016.09.001.

[47] L. Xu, X. Fu, G. Zha, T. Wang, Y. Xu, W. Jie, Effects of IR irradiation on the transport properties through deep-level defects in CdZnTe crystals studied by thermally stimulated current, J. Cryst. Growth, 468 (2017) 749-752, doi: 10.1016/j.jcrysgro.2016.09.065.

[48] B. Zhou, W. Jie, T. Wang, L. Xu, F. Yang, L. Yin, X. Fu, R. Nan, Studies on the deep-level defects in CdZnTe crystals grown by travelling heater method, Phys. Status Solidi A, 214 (2017) 1600748, doi: 10.1002/pssa.201600748.

[49] X. Fu, Y. Xu, Y. Gu, N. Jia, L. Xu, G. Zha, T. Wang, W. Jie, Study on the effects of indentation-induced dislocations on the detector performance of CdZnTe crystals, J. Appl. Phys., 122 (2017) 225102, doi: 10.1063/1.5002761.

[50] R. Nan, T. Li, Z. Jian, G. Xu, X. Li, Macroscopic effects and microscopic origins of gamma-ray irradiation on In-doped CdZnTe crystal, J. Mater. Sci. Mater. Electron., 29 (2018) 20462-20469, doi: 10.1007/s10854-018-0180-0.

[51] X. Fu et al., Distinctive distribution of defects in CdZnTe: In ingots and their effects on the photoelectric properties, Chin. Phys. B, 27 (2018) 037302, doi: 10.1088/1674-1056/27/3/037302.

[52] L. Bao, G. Zha, L. Xu, B. Zhang, J. Dong, Y. Li, W. Jie, Neutron irradiation-induced defects in $Cd_{0.9}Zn_{0.1}Te$: In crystals, Mater. Sci. Semicond. Process., 100 (2019) 179-184, doi: 10.1016/j.mssp.2019.05.002.

[53] T. Wang, X. Ai, Z. Yin, Q. Zhao, B. Zhou, F. Yang, L. Xu, G. Zha, W. Jie, Study on a co-doped CdZnTe crystal containing Yb and In, CrystEngComm, 21 (2019) 2620-2625, doi: 10.1039/C8CE02032A.

[54] L. Xu, W, Jie, Deep-level defect effects on the low-temperature photoexcitation process in CdZnTe crystals, J. Electron. Mater., 49 (2020) 429-434, doi: 10.1007/s11664-019-07721-6.

[55] V. Babentsov, J. Franc, E. Dieguez, M. V. Sochinskyi, R. B. James, Unique Deep Level in Spectroscopic CdZnTe: Compensation, Trapping, and Polarization, IEEE Trans. Nucl. Sci., 59 (2012) 1531-1535, doi: 10.1109/TNS.2012.2191159.

[56] A. Musiienko, R. Grill, P. Hlídek, P. Moravec, E. Belas, J. Zázvorka, G. Korcsmáros, J. Franc, I. Vasylchenko, Deep levels in high resistive CdTe and CdZnTe explored by photo-Hall effect and photoluminescence spectroscopy, Semicond. Sci. Technol., 32 (2016) 015002, doi: 10.1088/0268-1242/32/1/015002.

[57] J. Szatkowski, E. P. -Popko, A. Hajdusianek, S. Kuźmiński, B. Bieg, P. Becla, Deep Level Transient Spectroscopy Studies of CdMnTe, Acta Phys. Pol. A, 87 (1995) 387-390, doi: 10.12693/APhysPolA.87.387.

[58] J. Szatkowski, E. P. -Popko, A. Hajdusianek, B. Bieg, Deep electron states in gallium-doped CdMnTe mixed crystals, J. Cryst. Growth, 161 (1996) 282-285, doi: 10.1016/0022-0248(95)00671-0.

[59] J. Szatkowski, E. P. -Popko, K. Sieranski, A. Hajdusianek, P. Becla, Indium-doped $Cd_{0.8}Mn_{0.2}Te$: DLTS study, Proc. SPIE, 3724 (1999)150-155, doi: 10.1117/12.342980.

[60] J. Szatkowski, E. P. -Popko, K. Sieranski, B. Bieg, Defect studies in $Cd_{0.95}Mn_{0.05}Te$: Ga by DLTS, J. Cryst. Growth, 197 (1999) 684-687, doi: 10.1016/S0022-0248(98)00965-8.

[61] E. P. -Popko, J. Szatkowski, K. Sierański, J. Fiałkowski, J. M. Wróbel, P. Becla, DX centers in indium-doped $Cd_{0.9}Mn_{0.1}Te$, Opt. Mater., 18 (2001) 163-165, doi: 10.1016/S0925-3467(01)00158-6.

[62] E. P. -Popko, J. M. Wrobel, A. Gubański, J. Fiałkowski, J. Szatkowski, K. Sierański, P. Becla, Electron trap energy levels in indium doped $Cd_{0.85}Mn_{0.15}Te$, AIP Conf. Proc., 893 (2007) 235-236, doi: 10.1063/1.2729855.

[63] K. H. Kim, A. E. Bolotinikov, G. S. Camarda, A. Hossain, R. Gul, G. Yang, Y. Cui et al, Defect levels of semi-insulating CdMnTe: In crystals, J. Appl. Phys., 109 (2011) 113715, doi: 10.1063/1.3594715.

[64] K. Kim, G. Jeng, P. Kim, J. Choi, A. E. Bolotnikov, G. S. Camarda, R. B. James, Influence of the cooling scheme on the performance and presence of carrier traps for CdMnTe detectors, J. Appl. Phys., 114 (2013) 063706, doi: 10.1063/1.4817869.

[65] X. Wen, J. Zhang, Y.Mao, J. Min, X. Liang, J. Huang, K. Tang, L. Wang, Investigation of point defects and electrical properties of the In-doped CdMnTe grown by traveling heater method, J. Cryst. Growth, 463 (2017) 79-85, doi: 10.1016/j.jcrysgro.2017.01.059.

[66] J. M. Wrobel, A. Gubański, E. P. -Popko, J. Rezmer, P. Becla, Thermally stimulated current in high resistivity $Cd_{0.85}Mn_{0.15}Te$ doped with indium, J. Appl. Phys.103, (2008) 063720, doi: 10.1063/1.2894576.

[67] L. Luan, Y. He, D. Zheng, L. Gao, H. Lv, P. Yu, T. Wang, Defects, electronic properties, and α particle energy spectrum response of the $Cd_{0.9}Mn_{0.1}Te$: V single crystal, J. Mater. Sci.: Mater. Electron. 31, (2020) 4479-4487, doi: 10.1007/s10854-020-02996-6.

[68] X. Mathew, Photo-induced current transient spectroscopic study of the traps in CdTe, Sol. Energy Mater. Sol. Cells, 76 (2003) 225-242, doi: 10.1016/S0927-0248(02)00276-3.

[69] Z. C. Huang, K. Xie, C. R. Wie, A simple and reliable method of thermoelectic effect spectroscopy for semi-insulating III-V semiconductors, Rev. Sci. Instrum., 62 (1991) 1951-1954, doi: 10.1063/1.1142398.

[70] S. A. Awadalla, A. W. Hunt, K. G. Lynn, H. Glass, C. Szeles, S. H. Wei, Isoelectronic oxygen-related defect in CdTe crystals investigated using thermoelectric effect spectroscopy, Phys. Rev. B - Condens. Matter Mater. Phys., 69 (2014) 1-4, doi: 10.1103/PhysRevB.69.075210.

[71] U. V. Desnica, M. Pavlović, Z-Q. Fang, D. C. Look, Thermoelectric effect spectroscopy of deep levels in semi-insulating GaN, J. Appl. Phys., 92 (2002) 4126-4128, doi: 10.1063/1.1504168.

[72] Y. Cui, G. W. Wright, X. Ma, K. Chattopadhyay, R. B. James, A. Burger, DC photoconductivity study of semi-insulating $Cd_{1-x}Zn_xTe$ crystals, J. Electron. Mater., 30 (2001) 774-778, doi: 10.1007/BF02665871.

[73] A. Burger, M. Groza, Y. Cui, U. N. Roy, M. Guo, Research on CdZnTe and other novel room temperature gamma ray spectrometer materials, Technical Report No. DOE/ID/14555, Fisk University, 2007.

[74] Y. Ling, J. Min, X. Liang, J. Zhang, L.Yang, Y. Zhang, M. Li, Z. Liu, and L. Wang, Carrier transport performance of $Cd_{0.9}Zn_{0.1}Te$ detector by direct current photoconductive technology, J. Appl. Phys., 121 (2017) 034502, doi: 10.1063/1.4974201.

[75] Y. Mao, J. Zhang, L. Lin, J. Lai, J. Min, X. Liang, J. Huang, K. Tang, L. Wang, Study on the mechanism of using IR illumination to improve the carrier transport performance of CdZnTe detector, Semicond. Sci. Technol., 33 (2018) 045002, doi: 10.1088/1361-6641/aab01e.

[76] General Electric Healthcare Israel, 98 Yigal Alon St. Tel Aviv, 6789141.

[77] Description of Boxcar and lock in algorithms in DLTS measurements, available at http://info.ifpan.edu.pl/Dodatki/WordPress/laplacedlts/?page_id=374; [accessed 23 March 2021).

[78] P. V. Raja, N. V. L. N. Murty, Electrically active defects in neutron-irradiated HPSI 4H-SiC X-ray detectors investigated by ZB-TSC technique, IEEE Trans. Nucl. Sci., 64 (2017) 23772385, doi: 10.1109/TNS.2017.2720192.

[79] P. V. Raja, M. Bouslama, S. Sarkar, K. R. Pandurang, J. -C. Nallatamby, N. DasGupta, A. DasGupta, Deep-Level Traps in AlGaN/GaN-and AlInN/GaN-Based HEMTs with different buffer doping technologies, IEEE Trans. Electron Devices, 67 (2020) 2304-2310, doi: 10.1109/TED.2020.2988439.

[80] P. V. Raja, N. V. L. N. Murty, D-T Neutron and ^{60}Co-gamma irradiation effects on HPSI 4H-SiC photoconductors, IEEE Trans. Nucl. Sci., 65 (2018) 558-565, doi: 10.1109/TNS.2017.2778299.

[81] D. K. Schroder, Semiconductor Material and Device Characterization, 3rd ed., IEEE John Wiley & Sons, New Jersy, 2006.